optica

Large-scale optical phased array using a low-power multi-pass silicon photonic platform: supplementary material

STEVEN A. MILLER,[1,†] YOU-CHIA CHANG,[1,2,†] CHRISTOPHER T. PHARE,[1] MIN CHUL SHIN,[1] MOSHE ZADKA,[1] SAMANTHA P. ROBERTS,[1] BRIAN STERN,[1] XINGCHEN JI,[1] ASEEMA MOHANTY,[1] OSCAR A. JIMENEZ GORDILLO,[1] UTSAV D. DAVE,[1] AND MICHAL LIPSON[1,*]

[1]Department of Electrical Engineering, Columbia University, New York, New York 10027, USA
[2]Department of Photonics and Institute of Electro-Optical Engineering, National Chiao Tung University, Hsinchu 30010, Taiwan
[†]contributed equally to work

*Corresponding author: ml3745@columbia.edu

This document provides supplementary information to "Large-scale optical phased array using a low-power multi-pass silicon photonic platform," https://doi.org/10.1364/OPTICA.7.000003.

1. High fabrication tolerance achieved using adiabatic directional couplers.

By using adiabatic directional couplers, we show this platform can achieve a high tolerance to fabrication variation and can thus achieve broadband low insertion loss. In contrast to traditional interference-based directional couplers [1–3] for spatial mode conversion, adiabatic directional couplers [4–7] do not require precise phase matching and exact length. In adiabatic couplers, the local effective refractive index n_{eff} of the modes is tuned adiabatically by tapering the widths of the two coupled waveguides. By tapering each of the waveguides in opposite directions, we ensure that the modes of the two individual waveguides have the same n_{eff} somewhere along the center of the coupler. These two individual modes couple and form supermodes (S1 and S2). In contrast to a traditional interference-based directional coupler, in which both supermodes are excited and interfere with each other, only one of the supermodes is excited in an adiabatic directional coupler. As an example, we show in Fig. S1(b) an adiabatic directional coupler that couples the TE_3 mode of the bus waveguide (TE_3^{bus}) to the TE_0 mode of the access waveguide (TE_0^{access}). Fig. S1(a) shows the local effective refractive index $n_{eff}(z)$ at each cross section along the directional coupler. One can see that the n_{eff} of the two individual modes (TE_3^{bus} and TE_0^{access}) cross each other at the center of the

directional coupler, resulting in an anticrossing between the supermode S1 and S2. Fig. S1(c) shows the mode profile of the super mode S1, which evolves from the TE_3^{bus} mode at the input to the TE_0^{access} mode at the output. We simulate the coupling efficiency of each adiabatic directional coupler (see Section 2), from which we calculate the insertion losses of the multi-pass structures in the presence of dimensional variation, as shown in Fig. S2(a). The simulated insertion losses remain less than 0.6 dB, 1.5 dB, and 2.8 dB for the 3-pass, 5-pass and 7-pass structures, respectively, if the dimensional variation is controlled within ± 15 nm. Our simulation shows that the insertion loss of the 7-pass structure can potentially be reduced to only 2 dB if the fabrication variations in all the geometries are kept within ± 11 nm. This large tolerance of our platform is in stark contrast to the sub-nanometer tolerance required in resonators. Although resonators can also enable low-power devices via light circulation, the resonance is unpredictable due to tight fabrication tolerance, strong temperature sensitivity, and narrow optical bandwidth. Resonators therefore require active compensation to align the resonance with the laser frequency. Our platform, in contrast, requires no active compensation since its tolerance is practically achievable in both electron beam and deep ultraviolet lithography [8]. We show in Fig. S2(b) the simulated insertion losses of the multi-pass structures at different wavelengths. All structures show theoretical 3-dB bandwidths exceeding 200 nm. The large
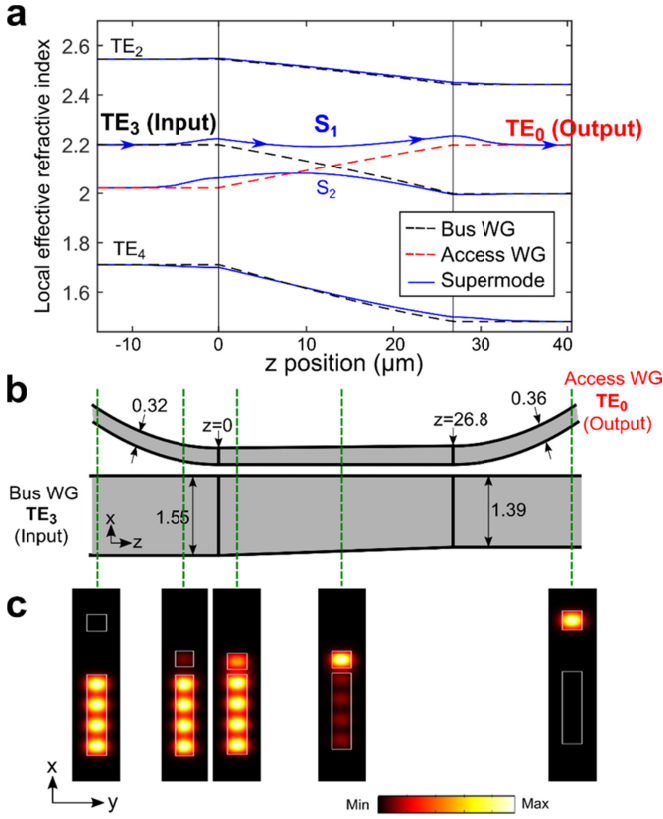
Fig. S1. | Design of the mode-selective adiabatic directional coupler. a. The local effective refractive indices $n_{eff}(z)$ at each cross section of the TE_3^{bus}-to-TE_0^{access} adiabatic directional coupler. One can see that the $n_{eff}(z)$ of the two individual waveguide (in the absence of the other waveguide) (black and red dashed lines) cross at the center of the directional coupler. The $n_{eff}(z)$ of the supermodes of the coupled waveguide system is also shown (blue). **b.** Schematic of the TE_3^{bus}-to-TE_0^{access} adiabatic directional coupler. The access waveguide and the bus waveguide are tapered linearly in opposite directions. **c.** Mode profile of the supermode S1 at different cross sections along the z position (indicated by the green dashed lines in **b**. The colour represents the energy density of the mode. The cross sections of the waveguides are indicated by white lines.

fabrication tolerance and high bandwidth are enabled by our design of adiabatic directional couplers and cannot be achieved with traditional interference-based directional couplers. By taking advantage of the lowered dispersion of subwavelength waveguides with an optimized adiabatic transition [13], the insertion loss could be further reduced to 2 dB for the 7-pass structure across ± 15 nm of dimensional variation (Fig. S2(c)).

For comparison, we simulate an alternative design of multi-pass structures that uses interference-based directional couplers instead of adiabatic directional couplers. In Table S1 and S2 we show the dimensions of the adiabatic and the interference-based directional couplers we use in the simulation. In Fig. S7 we show the performance of this alternative design. In stark contrast to the
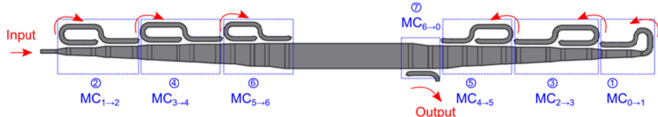

Fig. S3. | Schematic (not to scale) of a 7-pass multi-pass structure that utilizes the seven modes from the TE_0 to the TE_6 mode. The labels of ① to ⑦ represent of the order of multi-pass sequence. $MC_{i \to j}$ represents the mode converter that converts the TE_i mode to the TE_j mode.

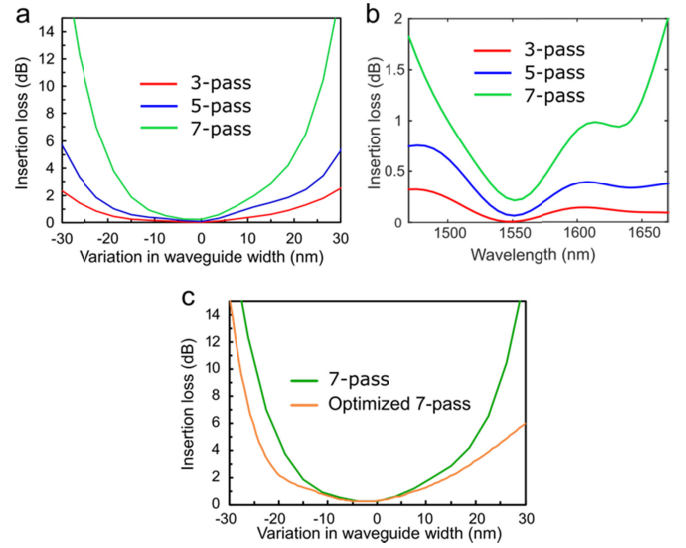**Fig. S2. | Simulated tolerance to fabrication-induced geometrical changes and bandwidth of the 3-pass, 5-pass and 7-pass multi-pass structures. a.** Simulated insertion losses as functions of the variation in the access waveguide width, the dimension that induces the largest insertion loss variation. The insertion losses remain less than 2.8 dB for a variation of ± 15 nm, indicating good tolerance to fabrication variation. **b.** Simulated insertion losses as functions of wavelength, assuming no dimensional variation. It shows that the 3-dB bandwidths of all multi-pass structures exceed 200 nm. **c.** Simulated insertion losses as functions of the variation in the access waveguide width. The insertion loss of the optimized 7-pass structure performs much better than the standard 7-pass structure and remains less than 3 dB for a variation of ± 20 nm, indicating better tolerance to fabrication variation.

adiabatic design, the 7-pass multi-pass structure using traditional interference-based directional couplers has a high insertion loss of 15.3 dB with the same dimensional variation of ± 15 nm and a 3-dB bandwidth of only 45 nm.

2. Multi-pass Device Simulation.

We simulate the effective refractive indices of the waveguides with the finite-element method using the commercial package COMSOL Multiphysics 5.1. The local effective refractive indices shown in Fig. S1(a) are simulated with the waveguide cross section at each z position along the directional coupler. We simulate the coupling efficiencies of the directional couplers with the commercial package Fimmwave 6.4. We also use Fimmwave to ensure that the tapers and the bends of the adiabatic directional couplers vary slowly enough to satisfy the adiabatic condition. We confirm that almost all the power is in one supermode as light propagates along the directional coupler, and the mode profile of this supermode evolves completely from one waveguide to another (as in Fig. S1(c)). We calculate the insertion loss of the multi-pass structure from the product of the coupling efficiencies of all individual directional couplers. The detailed dimensions of the devices we
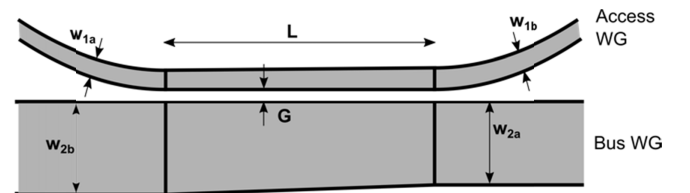

Fig. S4. | Schematic of a directional coupler. The dimensions are given in Table S1 and S2.

use in the simulation are given in Table S1. Unless stated otherwise, we perform the simulations at the wavelength of 1550 nm.

3. Theoretical enhancement factor of the multi-pass phase shifters.

In the multi-pass phase shifters, the phase shift is enhanced because the light passes through the same heated waveguide multiple times. The total phase shift is the sum of the phase shift seen by the light in each pass. However, because in each pass the light passes with a different mode, it sees a slightly different phase shift. We use the finite-element method to simulate $dn_{eff,m}/dT$ for all modes. Here $n_{eff,m}$ denotes the effective refractive index of the TE_{m-1} mode, and T is the temperature. We perform the simulation at the wavelength of 1600 nm. The thermo-optic coefficients of Si and SiO$_2$ used in the simulation are 1.86×10^{-4} and 9.5×10^{-6} respectively [9,10]. For a silicon waveguide with a cross section of 2.44 μm × 0.25 μm, we obtain $dn_{eff,m}/dT$ of 1.883×10^{-4}, 1.916×10^{-4}, 1.976×10^{-4}, 2.069×10^{-4}, 2.207×10^{-4}, 2.407×10^{-4}, and 2.641×10^{-4} for the TE_0 to TE_6 mode, respectively. One can see that the higher-order modes have slightly larger $dn_{eff,m}/dT$ due to stronger dispersion. The theoretical enhancement factor for an n-pass phase shifter is given by

$$\left[\sum_{m=1}^{n}\left(\frac{dn_{eff,m}}{dT}\right)\right]/\frac{dn_{eff,1}}{dT} \quad \text{(S1)}$$

We obtain the theoretical enhancement factor for the 3-pass, 5-pass and 7-pass phase shifters, which are 3.07, 5.34 and 8.02 respectively. Note that this analysis considers only the phase shift created in the waveguide section that is directly under the resistive heater. Other nearby waveguide sections also have a small temperature increase and therefore contribute to the phase shift. We attribute the small deviation between the measured and theoretical enhancement factors to such contribution.

4. Free spectral range of the Mach-Zehnder interferometers with multi-pass structures.

We confirm light circulation by measuring the free spectral range (FSR) of the Mach-Zehnder interferometers (MZIs) with multi-pass structures. Because light circulates multiple times in the multi-pass structure, the optical path length of the multi-pass arm becomes longer than the physical length. The FSR of a MZI is given by $\lambda^2/\Delta OPL$, where ΔOPL is the optical path difference between the two interferometer arms [11]. Because of light circulation, the MZI has a larger ΔOPL and therefore a smaller FSR compared to a MZI without light circulation. We measure the transmission spectra of the MZIs with different number of passes, as shown in the inset of Fig. 2 of the main text. The measured FSR of the MZI interference fringes near the wavelength 1600 nm are 0.461 nm, 0.214 nm, and 0.141 nm for the 3-pass, 5-pass, and 7-pass MZIs, respectively. The measured FSR decreases with the number of passes, indicating an increase of ΔOPL.

To confirm the mechanism, we calculate the theoretical FSR of each MZI from the optical path length of our design and compare with the experimental results. The optical path length is given by $\int n_g(l)dl$, where n_g is the group index. The group index depends on the dimensions and the mode of a waveguide. We use the finite-element method to simulate the group index of the relevant modes
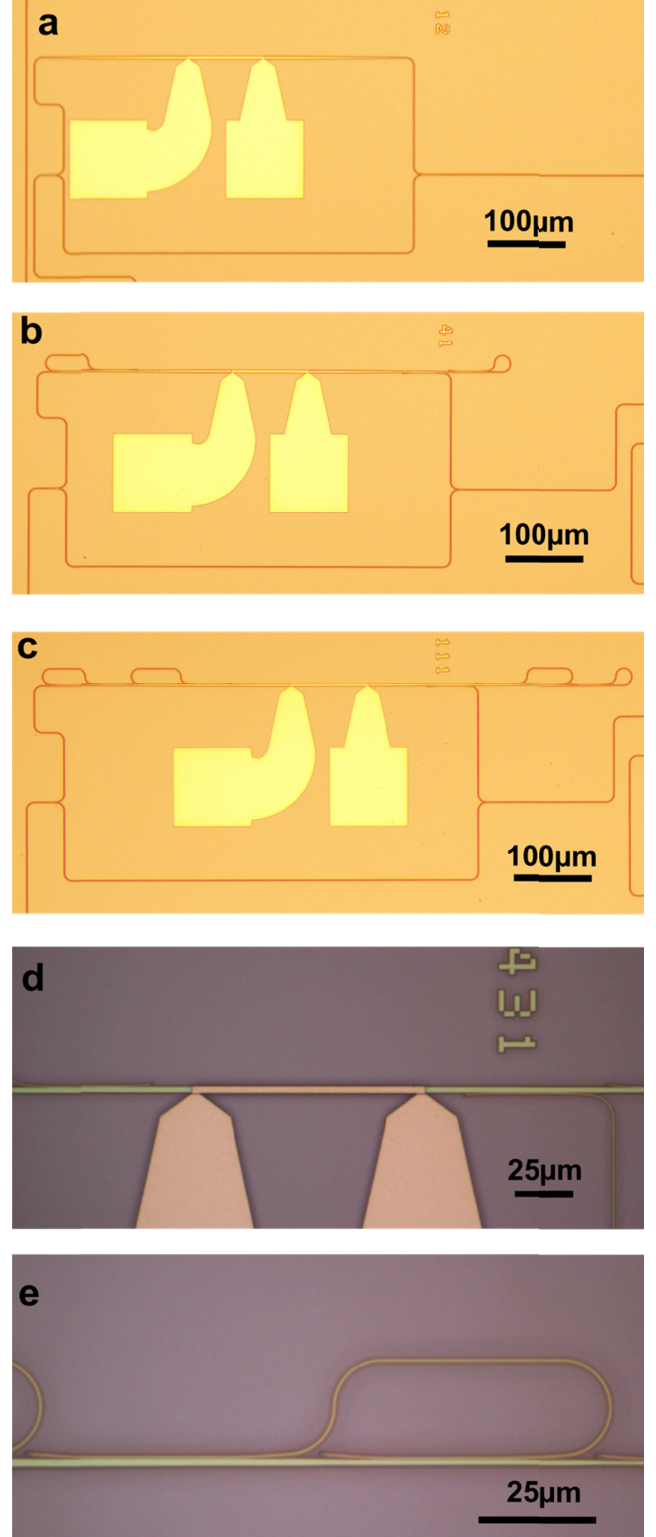

Fig. S5. | Optical microscope images of the Mach-Zehnder interferometers with different multi-pass structures. a. The standard MZI without multi-pass structure. **b.** The MZI with the 3-pass multi-pass structure. **c.** The MZI with the 5-pass multi-pass structure. **d.** The resistive heater in the 7-pass multi-pass structure. **e.** The TE_2-to-TE_3 mode converter in the 7-pass multi-pass structure.

of the designed waveguides. We integrate the group index along the path that light circulates. The theoretical FSR near the wavelength of 1600 nm are 0.472 nm, 0.206 nm, and 0.145 nm for
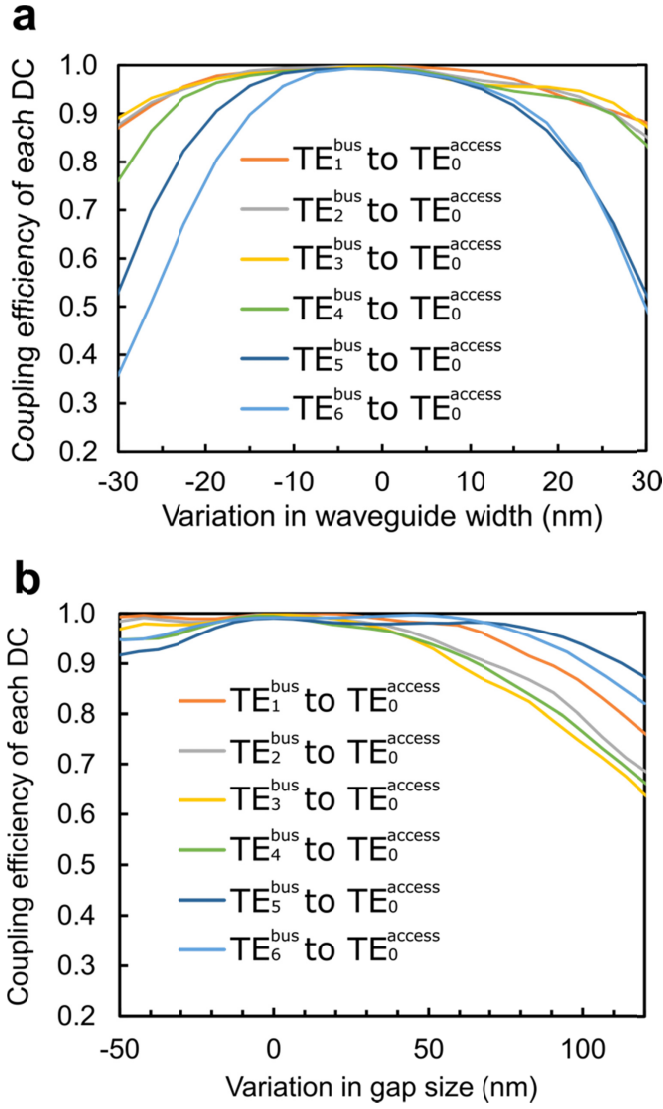
Fig. S6. | **Simulated dimensional tolerance of different mode-selective adiabatic directional couplers. a.** The tolerance to the waveguide width variation. In this simulation, we give the same variation to the access waveguide widths w_{1a} and w_{1b}, which are the most crucial dimensions. The coupling efficiencies remains > 90% within a variation of ± 15 nm, indicating good tolerance to fabrication variation. The higher-order mode directional couplers are less tolerant due to smaller n_{eff} difference between modes. The notations w_{1a} and w_{1b} are defined in Fig. S4. **b.** The tolerance to the gap size between the waveguides. Adiabatic directional couplers are robust with respect to the gap size variation. The coupling efficiencies remain > 91% within a gap size variation of ± 50 nm. The detailed dimensions can be found in Table S1.

the 3-pass, 5-pass, and 7-pass MZIs, respectively. The good agreement between the measured and theoretical FSR confirms the mechanism of mode conversion and light circulation. We attribute the small deviation (less than 4 %) to the non-perfect dimension in actual fabrication.

5. Eye diagram of signals through the multi-pass structure.

We demonstrate that the multi-pass structure can be used for communication applications. We send 10-Gb/s data through the 7-pass multi-pass structure. As shown by Fig. S10, we modulate the laser with 2^7-1 pseudo-random binary sequence (PRBS) using
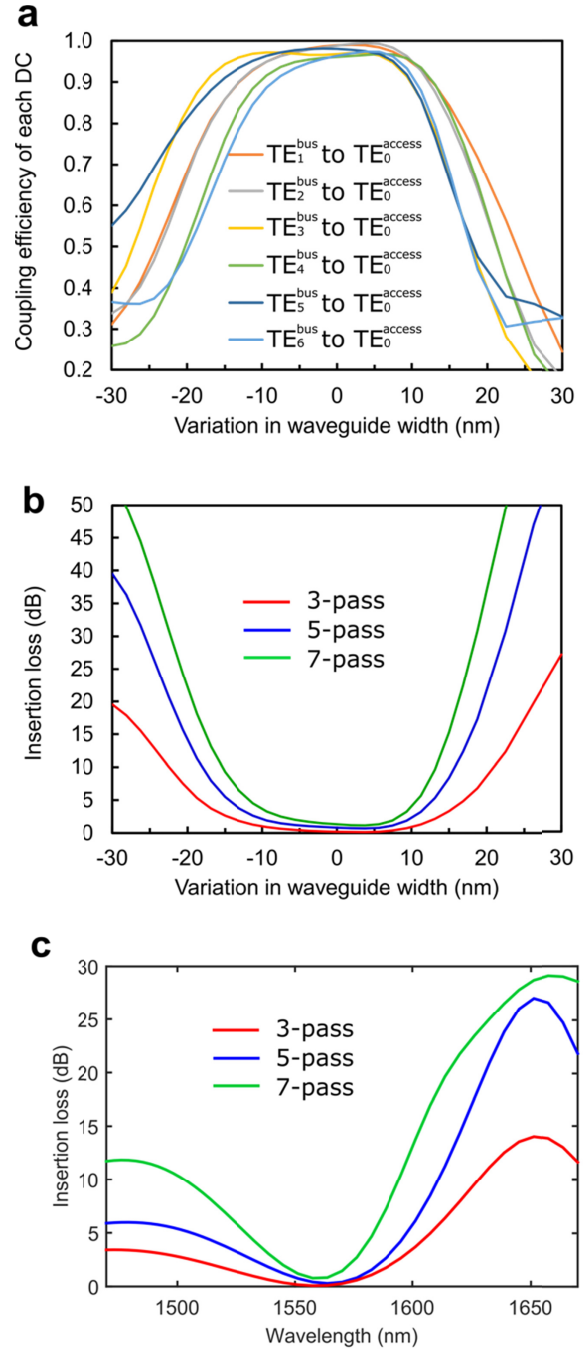

Fig. S7. | **Simulated performance of interference-based directional couplers. a.** Simulated coupling efficiencies of each interference-based directional couplers (as opposed to the adiabatic couplers we use) as functions of the variation in the access waveguide width. The detailed dimensions of these directional couplers are given in Table S2. **b.** Simulated tolerance of the multi-pass structures that use the interference-based directional couplers. **c.** Simulated insertion loss spectra of the multi-pass structures that use the interference-based directional couplers. We perform this simulation to draw a comparison between the adiabatic directional couplers and the traditional interference-based directional couplers. The simulation shows that the interference-based directional couplers are less tolerant to fabrication variation compared to the adiabatic counterpart. The coupling efficiency can decrease to 66 % when there is a dimensional variation of ± 15 nm. The 3-dB optical bandwidths of the 3-pass, 5-pass and 7-pass multi-pass structures that use the interference-based directional couplers are 110 nm, 65 nm and 45nm, respectively, which are much narrower than the adiabatic design.

a LiNbO$_3$ amplitude modulator. The measured eye diagram through the 7-pass multi-pass structure is clearly open and shows
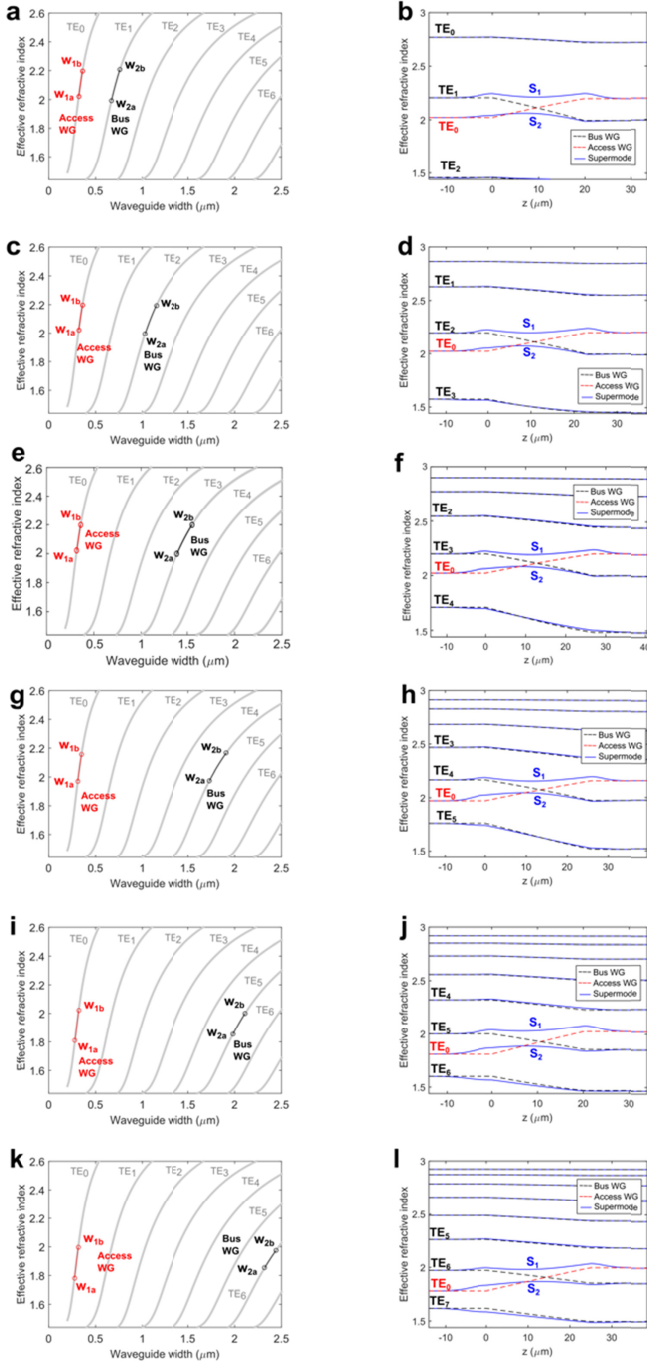
Fig. S8. | Local effective refractive indices of the adiabatic directional couplers designed for different modes. a,c,e,g,i,k. The simulated n_{eff} of different waveguide modes as functions of the waveguide width, showing the ability to engineer the n_{eff} by controlling the waveguide width1-3. The widths used in the TE_1^{bus}-to-TE_0^{access}, TE_2^{bus}-to-TE_0^{access}, TE_3^{bus}-to-TE_0^{access}, TE_4^{bus}-to-TE_0^{access}, TE_5^{bus}-to-TE_0^{access}, TE_6^{bus}-to-TE_0^{access} adiabatic directional coupler are marked in (a), (c), (e), (g), (i), (k), respectively. We take advantage of the high index contrast in silicon waveguides, which leads to the large separation between the n_{eff} of different modes. **b,d,f,h,j,l.** The simulated local effective refractive indices $n_{eff}(z)$ at each cross section in the adiabatic directional couplers. The $n_{eff}(z)$ of the TE_1^{bus}-to-TE_0^{access}, TE_2^{bus}-to-TE_0^{access}, TE_3^{bus}-to-TE_0^{access}, TE_4^{bus}-to-TE_0^{access}, TE_5^{bus}-to-TE_0^{access}, TE_6^{bus}-to-TE_0^{access} adiabatic directional couplers are shown in (b), (d), (f), (h), (j), (l), respectively. The $n_{eff}(z)$ of the two individual waveguides (in the absence of the other waveguide) is plotted as black and red dashed lines. We achieve mode selectivity by allowing only one crossing between the red and black dashed lines. The $n_{eff}(z)$ of the supermodes of the coupled waveguide system is plotted as blue solid lines. The notations of waveguide widths are defined in Fig. S4. The detailed dimensions of the adiabatic directional couplers are given in Table S1.
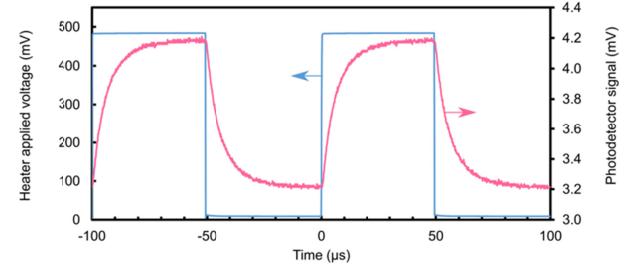

Fig. S9. | The temporal response of the thermo-optic phase shifter with the 7-pass multi-pass structure. The thermal time constant is obtained by fitting the photodetector signal with an exponential function. We find that the thermal time constant is independent of the number of passes. In all 1-pass, 3-pass, 5-pass and 7-pass devices, we measure thermal time constants of 6.4 ± 0.2 μs (rise time) and 6.6 ± 0.4 μs (fall time).

no significant degradation in performance compared to the back-to-back eye diagram excluding the chip. This confirms that the mode conversion in our approach does not limit the bandwidth and can potentially be used to enhance the tunability of high-speed modulators.

6. Wavelength dependence of the phase shift induced by the multi-pass phase shifter.

The phase shift enhanced by our approach is broadband. This is because the enhancement is achieved by passing the light through the same heated waveguide multiple times with different modes. The only contribution to the wavelength-dependent phase shift is the weak mode dispersion of the multimode waveguide section directly under the heater. This is in contrast to the resonator-based approach, in which the phase shift is strongly wavelength dependent because the enhancement occurs only near resonance. As shown by Fig. S11(a), one can see from the measured 7-pass multi-pass phase shifter at 1 mW heater power at four different wavelengths from 1525 nm to 1600 nm, that the phase shift varies only by 3.7 % over this 75 nm of spectral range. We also plot the simulated phase shift in the same figure, which is obtained from

$$\Delta\phi(\lambda) = \frac{2\pi}{\lambda}\sum_{m=1}^{7}\left(\frac{dn_{eff,m}}{dT}\right)\Delta T\ L \qquad (S2)$$
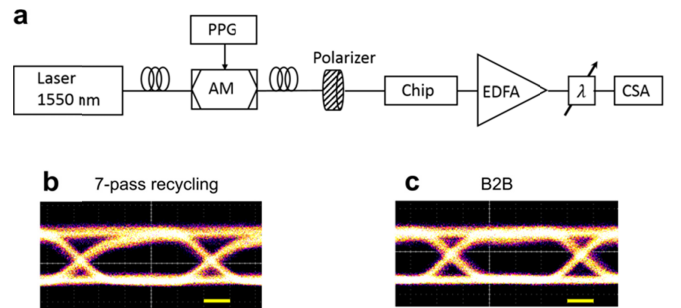

Fig. S10. | Eye diagram of signals through the multi-pass structure. a. Test setup, including laser, LiNbO₃ amplitude modulator (AM), pulsed pattern generator (PPG), fiber polarizer, Erbium-doped fiber amplifier (EDFA), tunable filter (λ), and communications signal analyzer (CSA). The amplitude modulator produces 10-Gb/s data with 2^7-1 pseudo-random binary sequence (PRBS). **b.** Eye diagram of signals through the 7-pass multi-pass structure shown in Fig. 1a of the main text. **c.** Eye diagram of the back-to-back (B2B) signals measured with the same setup without the chip. Scale bar: 20 ps.
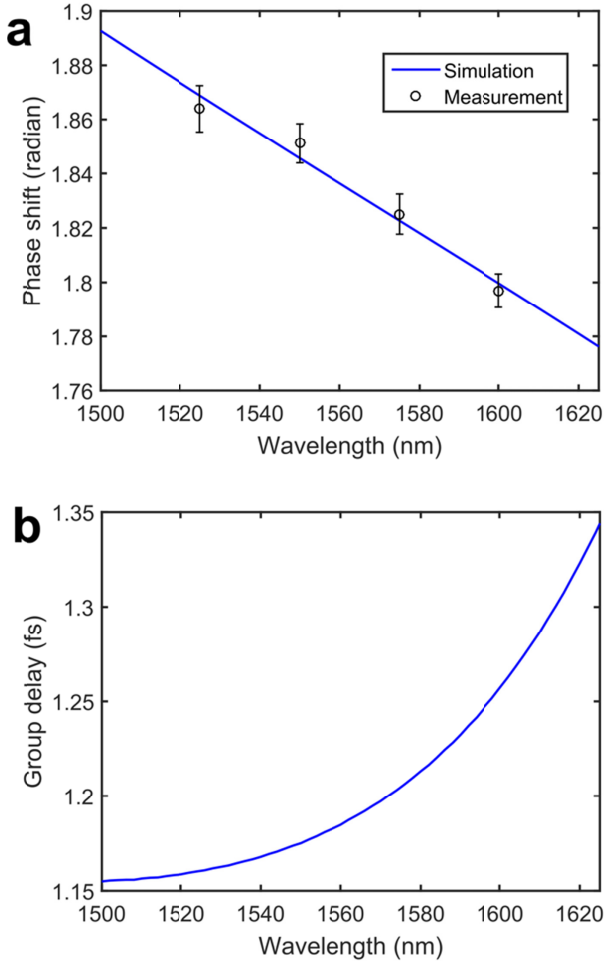
Fig. S11. | Wavelength dependence of the phase shift induced by the multi-pass phase shifter. a. Phase shift induced by the 7-pass multi-pass phase shifter operated at 1 mW heater power. The measured phase shift varies only by 3.7 % over the spectral range from 1525 nm to 1600 nm. This demonstrates broadband phase shift enhancement, in contrast to the strongly wavelength-dependent enhancement in the resonator-based approach. The simulation reproduces the measurement well. **b.** Simulated group delay induced by the 7-pass multi-pass phase shifter operated at 1 mW heater power.

where ΔT is the temperature change created by the heater. L is the length of the heated section of the waveguide. $\frac{dn_{eff,m}}{dT}$ is obtained by the finite-element simulation for each mode and shows weak wavelength dependence. We use ΔT as the only parameter for fitting the measurement results. As shown by Fig. S11(a), the measured phase shift matches well with the simulation when ΔT=3.04 °C. This temperature change is also verified with the finite-element heat transfer simulation. Fig. S11(b) shows the simulated group delay $d(\Delta\phi)/d\omega$ as a function of wavelength.

7. Wavelength sensitivity of grating emission angle for vertical beam steering.

We are able to increase our vertical steering range by increasing the emission angle sensitivity. The wavelength sensitivity of the grating emission angle is a function of the nominal emission angle. By choosing a grating period of 520 nm, the beam emits nominally at a 45° angle around 1550nm wavelength, and we can achieve 0.265°/nm sensitivity, as seen in Fig. S13. This sensitivity
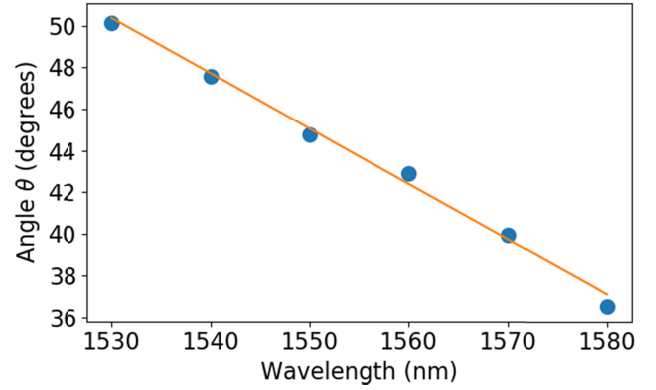

Fig. S12. | Wavelength sensitivity of grating emission angle for vertical beam steering. We measure the grating emission angle for different wavelengths using our Fourier transform imaging system (see Methods) for wavelengths between 1530 nm and 1580 nm. The line drawn is a linear fit corresponding to a slope of 0.265°/nm wavelength sensitivity.

corresponds to more than 26° of steering per 100nm of the input laser's wavelength tuning, doubling the usual angle sensitivity at longer grating periods. At this emission angle, the effective aperture size is the projection of our actual aperture at the emission angle, so our long grating length compensates for this small decrease.

8. Multipass Device Fabrication.

We fabricate the standalone multi-pass devices on a silicon-on-insulator (SOI) wafer from Soitec, which has a 250 nm top silicon layer and a 3 μm buried oxide layer. The silicon wire waveguides are patterned by electron beam lithography (Elionix ELS-G100) using ma-N 2403 e-beam resist, etched by inductively coupled plasma (ICP) using fluorine-based chemistry, and clad with 1 μm silicon dioxide (SiO_2) by plasma-enhanced chemical vapor deposition (PECVD). On top of the SiO_2 cladding, we fabricate 100 μm-long, 3 μm-wide resistive heaters as thermo-optic phase shifters. The heaters and the pads are patterned with electron beam lithography, followed by sputtering (5 nm Ti and 100 nm W) and lift-off.

9. Multi-pass Device Characterization.

We measure the transmission spectra of the multi-pass devices with a tunable laser source (Ando AQ4321D) that can sweep the wavelength from 1520 nm to 1620 nm. We couple the light into the chip and collect it from the chip with lensed fibers. The silicon waveguide is inversely tapered to a 160 nm width at the input and output facets to match the mode size of the lensed fibers. We use 1×2 multimode interference (MMI) couplers with 50/50 split ratio to split and recombine light in the MZI. The output power is detected by a power meter with an InGaAs detector (Newport 818-IG) when acquiring the device transmission spectra. Another InGaAs detector with a higher speed (Thorlabs PDB150C) is used when measuring the temporal response of the resistive heaters. The resistive heaters are driven with a source meter (Keithley 2400-LV) and a function generator in the phase shift and heater temporal response measurements, respectively. The resistance of the resistive heaters (excluding the contact resistance) range from 835 Ω to 983 Ω in our devices. We calculate applied heater power

from the measured current (with Keithley 2400-LV source meter) and from the resistance of each heater.

10. Extraction of the insertion loss from the visibility of interference fringes.

The insertion loss of the multi-pass structure is directly related to the visibility of the MZI interference fringes, assuming the splitters of the MZI have an accurate split ratio of 50/50. The visibility V of interference fringes is defined as $(P_{max} - P_{min})/(P_{max} + P_{min})$, where P_{max} and P_{min} are the power at the peak and the valley, respectively. The insertion loss in dB is given by $-log_{10}\{2[1 - \sqrt{(1 - V^2)}]/V^2 - 1\}$. We fit the acquired fringes locally with sine functions, extract the visibility, and calculate the insertion loss as a function of wavelength.

11. Phased Array Device Fabrication.

We fabricate the optical phased array on a silicon-on-insulator (SOI) wafer from Soitec with a 220 nm top silicon layer and 2 μm buried oxide layer. The silicon wire waveguides are patterned by electron beam lithography (Elionix ELS-G100) using ma-N 2403 photoresist, etched by inductively coupled plasma (ICP) using fluorine-based chemistry, and clad with 700 nm silicon dioxide (SiO₂) by plasma-enhanced chemical vapor deposition (PECVD). On top of the SiO₂ cladding, we fabricate 360 μm-long, 540 nm-wide resistive heaters as thermo-optic phase shifters. The metal is sputtered (5 nm Ti and 100 nm Pt) and the heaters are patterned using electron beam lithography followed by Argon ion milling. We fabricate two metal layers, (M1) for the wires and bond pads, and (M2) for a large common ground path. M1 is defined using a double layer of PMMA resist patterned in contact photolithography and a lift-off process. For M1, we sputter 10 nm of Ti followed by 700 nm of Al. We then clad with 1 μm of PECVD SiO₂ and etch vias down to connect M1 to M2. For M2, we use the same lift-off process, this time sputtering 10 nm of Ti followed by 1.5 μm of Al.

12. Phased Array Device Packaging.

We use a silicon interposer to route the dense array of electrical control signals out to external control circuitry. The silicon interposer is made using a virgin silicon wafer with 50 nm of silicon dioxide grown using dry thermal oxidation. Underneath the footprint of the phased array chip, a window is etched through the thermal oxide down to the silicon substrate using buffered oxide etch (BOE) 6:1 to allow for efficient thermal conduction between the phased array chip and the interposer. A thick metal interconnect layer is sputtered (10 nm Ti, 3 μm Al) and patterned in contact photolithography. The Al is etched using an ICP chlorine-base chemistry. The silicon interposer is attached to a PCB and the phased array chip is attached to the silicon interposer using thermally conductive epoxy. The chip is connected to the interposer with triple stacked gold wirebonds and the interposer is connected to the PCB with a single row of Al wirebonds. The PCB is mounted onto a heatsink.

13. Phased Array Device Characterization.

We characterize the phased array device using a tunable laser source (Ando AQ4321D) that can sweep the wavelength from 1520 nm to 1620 nm. We couple the light into the edge of the chip with a lensed fiber which is mode matched to a 180 nm wide silicon waveguide inverse taper. Light is emitted from the array of emitter gratings at a 45° angle. The far field image of the emitted beam is viewed using a Fourier transform imaging system. Additionally, a tilted mirror is placed above the chip to direct the emitted beam toward a single element, 1 mm diameter photodiode in the Fraunhofer far-field approximately 1 m away from the chip. The detector is connected to a lock-in amplifier. We use an on-chip thermo-optic MZI modulator with the lock-in amplifier to detect the emitted light from the phased array. We control each thermo-optic phase shifter using a National Instruments PXIe-6739 multi-channel analog output module. To align the phases of all the channels and form a beam centered on the fixed detector position, we run a global optimization algorithm [12]. In order to measure the 2D far-field emission pattern, we mount the mirror above the chip with a motorized tilt mount to sweep the vertical direction and a motorized rotation stage to sweep the horizontal direction and obtain a 2D scan of the emission pattern on the single element photodiode.

Table S1. The dimensions of the adiabatic directional couplers used in the multi-pass structure. The radius of the arc is 130 μm. The height of the silicon waveguide is 250 nm. Other notations are defined in Fig. S4.

Mode in the access waveguide	Mode in the bus waveguide	w_{1a} (μm)	w_{1b} (μm)	w_{2a} (μm)	w_{2b} (μm)	G (μm)	L (μm)
TE_0	TE_1	0.32	0.36	0.67	0.76	0.1	19.8
TE_0	TE_2	0.32	0.36	1.03	1.15	0.1	23
TE_0	TE_3	0.32	0.36	1.39	1.55	0.1	26.8
TE_0	TE_4	0.31	0.35	1.73	1.91	0.1	25.8
TE_0	TE_5	0.28	0.32	1.98	2.11	0.1	20.2
TE_0	TE_6	0.275	0.315	2.32	2.44	0.13	24.9

Table S2. The dimensions of an alternative design that uses interference-based directional couplers. We design these directional couplers to draw a comparison between the adiabatic and the traditional interference-based directional couplers. The bus waveguide is slightly tapered to relax the requirement of exact phase matching [4], but the coupling is not in the adiabatic regime. The radius of the arc is 40 μm. The height of the silicon waveguide is 250 nm. Other notations are defined in Fig. S4. The simulated performance of these directional couplers is shown in Fig. S7.

Mode in the access waveguide	Mode in the bus waveguide	w_{1a} (μm)	w_{1b} (μm)	w_{2a} (μm)	w_{2b} (μm)	G (μm)	L (μm)
TE_0	TE_1	0.39	0.39	0.77	0.85	0.1	17.4
TE_0	TE_2	0.39	0.39	1.18	1.3	0.1	21.6
TE_0	TE_3	0.39	0.39	1.58	1.74	0.1	23
TE_0	TE_4	0.36	0.36	1.89	2.05	0.1	19.8
TE_0	TE_5	0.35	0.35	2.15	2.43	0.1	30.1
TE_0	TE_6	0.33	0.33	2.47	2.71	0.1	30.1

References

1. J. Wang, S. He, and D. Dai, "On-chip silicon 8-channel hybrid (de)multiplexer enabling simultaneous mode- and polarization-division-multiplexing," Laser & Photonics Rev. **8**, L18–L22 (2014).

2. Y. Ding, J. Xu, F. D. Ros, B. Huang, H. Ou, and C. Peucheret, "On-chip two-mode division multiplexing using tapered directional coupler-based mode multiplexer and demultiplexer," Opt. Express **21**, 10376–10382 (2013).

3. A. Mohanty, M. Zhang, A. Dutt, S. Ramelow, P. Nussenzveig, and M. Lipson, "Quantum interference between transverse spatial waveguide modes," Nat. Commun. **8**, 14010 (2017).

4. N. Riesen, and J. D. Love, "Ultra-Broadband Tapered Mode-Selective Couplers for Few-Mode Optical Fiber Networks," IEEE Photonics Technol. Lett. **25**, 2501–2504 (2013).

5. X. Sun, H.-C. Liu, and A. Yariv, "Adiabaticity criterion and the shortest adiabatic mode transformer in a coupled-waveguide system," Opt. Lett. **34**, 280–282 (2009).

6. A. F. Milton, and W. K. Burns, "Tapered Velocity Couplers for Integrated Optics: Design," Appl. Opt. **14**, 1207–1212 (1975).

7. K. Solehmainen, M. Kapulainen, M. Harjanne, and T. Aalto, "Adiabatic and Multimode Interference Couplers on Silicon-on-Insulator," IEEE Photonics Technol. Lett. **18**, 2287–2289 (2006).

8. S. K. Selvaraja, W. Bogaerts, P. Dumon, D. V. Thourhout, and R. Baets, "Subnanometer Linewidth Uniformity in Silicon Nanophotonic Waveguide Devices Using CMOS Fabrication Technology," IEEE J. Sel. Top. Quantum Electron. **16**, 316–324 (2010).

9. G. Cocorullo, and I. Rendina, "Thermo-optical modulation at 1.5μm in silicon etalon," Electron. Lett. **28**, 83–85 (1992).

10. A. Arbabi, and L. L. Goddard, "Measurements of the refractive indices and thermo-optic coefficients of Si_3N_4 and SiO_x using microring resonances," Opt. Lett. **38**, 3878–3881 (2013).

11. A. Yariv, and P. Yeh, *Photonics: Optical Electronics in Modern Communications* (Oxford University Press, 2007).

12. C. T. Phare, M. C. Shin, S. A. Miller, B. Stern, and M. Lipson, "Silicon Optical Phased Array with High-Efficiency Beam Formation over 180 Degree Field of View," arXiv:1802.04624 (2018).

13. U. D. Dave, and M. Lipson, "Efficient Conversion to Very High Order Modes in Silicon Waveguides," in Conference on Lasers and Electro-Optics (CLEO), paper SM3J.6 (2019).